Bulletin of Geophysics and Oceanography Vol. 66, n. 4, pp. 389-404; December 2025
DOI 10.4430/bgo00511

The geoelectric coast effect: a stepped-depth sea model

G. Lucca

Independent researcher, Piacenza, Italy

(Received: 18 June 2025; accepted: 22 October 2025; published online: 12 December 2025)

ABSTRACT It is known that geoelectric fields, induced at ground level, during geomagnetic storms may represent a threat for infrastructures such as power lines, pipelines, and railway lines. Particularly, when one of these structures is located inside a region characterised by large lateral ground conductivity contrast (typically a coastal region where the seawater conductivity is significantly higher than that of the land), the commonly named geoelectric coast effect manifests and consists in an increased level of the induced geoelectric field near the coastline with penetration inside the land region for several kilometres. A convenient calculation method, capable of assessing the geoelectric coast effect, is the generalised thin sheet model. In literature, this method is generally applied by considering the idealised case of a constant-depth sea. On the contrary, in this paper, we extend its use to the more realistic case of a stepped-depth sea model. In such a way, we show that, by considering a shelf region, characterised by different sea depth levels and located between the coastline and the maximum sea depth region, the application of such model results in significant differences in the predicted geoelectric field with respect to the simpler constant-depth sea model. Moreover, the influence of certain parameters characterising the model (shelf region length and slope, and maximum sea depth) is put into evidence. These are the main novelties introduced by this paper.

Key words: geomagnetic storm, geoelectric coast effect, geoelectric field, generalised thin sheet model, geomagnetically induced currents.

1. Introduction

It is known that during a geomagnetic storm, the induced geoelectric field at Earth surface drives a geomagnetically induced current (GIC) that may couple with infrastructures such as power lines, telecommunication cables, pipelines, and railway lines resulting, in the case of strong storms, in a risk of disturbances, malfunctioning, or even severe damages to the above-mentioned plants (Boteler, 2001a, 2001b, 2003; Pilipenko, 2021).

The first necessary step to assess the GIC interfering with such structures, is the evaluation of the geoelectric field in the region where the involved structure is located. If such a region does not present significant conductivity variations in any horizontal direction but only in the vertical one (i.e. along the depth), then, the Earth can be approximated by means of a one-dimensional (1D) model. If this is not the case, then, a two-dimensional (2D) or three-dimensional (3D) model must be adopted to describe the Earth structure. A classic example is represented by coastal regions where a strong conductivity contrast exists between the seawater conductivity and that of the land. As a consequence of this large gap between the two conductivities, a significant

enhancement of the geoelectric field, perpendicular to the coastline, is produced on the land side (Fischer, 1979; Gilbert, 2005). This phenomenon represents the commonly called geoelectric coast effect.

The simplest case occurs when the conductivity depends only on one of the two horizontal coordinates and, in this case, a 2D model can be adopted for the geoelectric field; the typical example is represented by a long uniform and rectilinear coast (Weaver, 1994).

To estimate the impact of the geoelectric coast effect, different approaches can be found in literature: analytical and numerical.

The first approaches to the problem were analytical: worthy of mention is the vertical fault model of finite depth above a semi-infinite homogeneous substratum having zero or infinite conductivity (d'Erceville and Kunetz, 1962), the dike model (Rankin, 1962), and the infinite vertical fault model (Weaver, 1963). Further information about these models can be found in Blake (1968). The basic limitation, relevant to these analytic approaches, is that they are too idealistic especially for substratum modelling (perfectly insulating or perfectly conducting) or for sea modelling (infinite depth).

The numerical methods are much more flexible and overcome the limitations of the analytical methods since they enable to consider Earth models characterised by many layers with different values of conductivity; among them we can mention a Finite Difference Time Domain approach (Pokhrel *et al*., 2018) or a Galerkin Finite Element Method (FEM) model (Dong *et al*., 2015a, 2015b). The FEM approach has been applied by Liu *et al*. (2018) to estimate the risk related to a GIC for the nuclear power station at Ling'ao in the Guandong Province, located in the coastal region of China.

The study of the geoelectric coast effect can also be faced by means of another method, i.e. the generalised thin sheet approach that was introduced by Ranganayaki and Madden (1980). Even if it is an approximate method, it enables to overcome many of the limitations related to the above-mentioned analytical methods. This approach consists in assuming that the Earth structure is composed of two layers laid over a basement which can have a generic stratification; the first conductive layer is composed of sediments or seawater, while the second resistive layer is composed of rocks. In the Pipeline Research Council International report (Gummow *et al*., 2002), it has been shown how the generalised thin sheet method can be applied, by means of a simple 2D model, to study the geoelectric coast effect under the condition of H polarisation assumed by the driving geomagnetic field. Furthermore, Wang *et al*. (2023) showed that a very useful analogy can be established between the generalised thin sheet method and the transmission line theory. Lastly, Lucca (2024) extended this method also to the case of a generic polarisation, i.e. a combination of H and E polarisation (see Appendix A) of the driving geomagnetic field.

In most of the papers present in literature and relevant to the prediction of the geoelectric coast effect, the sea is modelled by means of a conductive layer having a fixed thickness, i.e. considering a constant-depth sea. Indeed, the sea depth increases gradually starting from the shore line up to the region where the depth is maximum; so, the question is what is the influence of this shelf zone, with a variable depth and located between the land side and sea region where the depth is maximum (deep-sea region), on the geoelectric field .

This paper presents a new theoretical approach based on the generalised thin sheet model, by introducing a stepped-depth sea model. This new approach was applied to synthetic examples and the results compared with the ones obtained by adopting the simpler constant-depth sea model. Additionally, the influence of the main parameters characterising the model (shelf region length and slope and maximum sea depth) was also thoroughly analysed.

2. Basic assumptions

In this section the basic assumptions for dealing with the case of a stepped-depth sea model, by exploiting the 2D basic model of Ranganayaki and Madden (1980), are described with the help of Fig. 1.

Let us assume that the coastal region under study is characterised by a long rectilinear and uniform coast along the *x*-axis (supposedly entering the sheet) and the driving geomagnetic field H_0 is constant over it; moreover, due to the uniformity of the coast, the physical parameters (e.g. the electrical conductivity) describing the Earth structure only depend on the *y* and *z* coordinates. Under these conditions, the same holds for induced electromagnetic field in both land and sea regions and, consequently, a 2D model can be applied.

In the frame of a 2D model and in the context of GIC evaluation on technological infrastructures, a simplified model of Earth stratification, like the one depicted in Fig. 1, can be assumed (Chakraborty *et al*., 2022; Boteler *et al*., 2023). By following the vertical direction along the *z*-axis, a simple representation of the Earth structure is obtained and it is given by a first conductive layer composed of sediments or seawater, then, a second resistive layer (crust), under which there is a more conductive common basement representing the Earth's stratified mantle (layers from 3 to *N*). Nevertheless, the model does not strictly request for the resistive

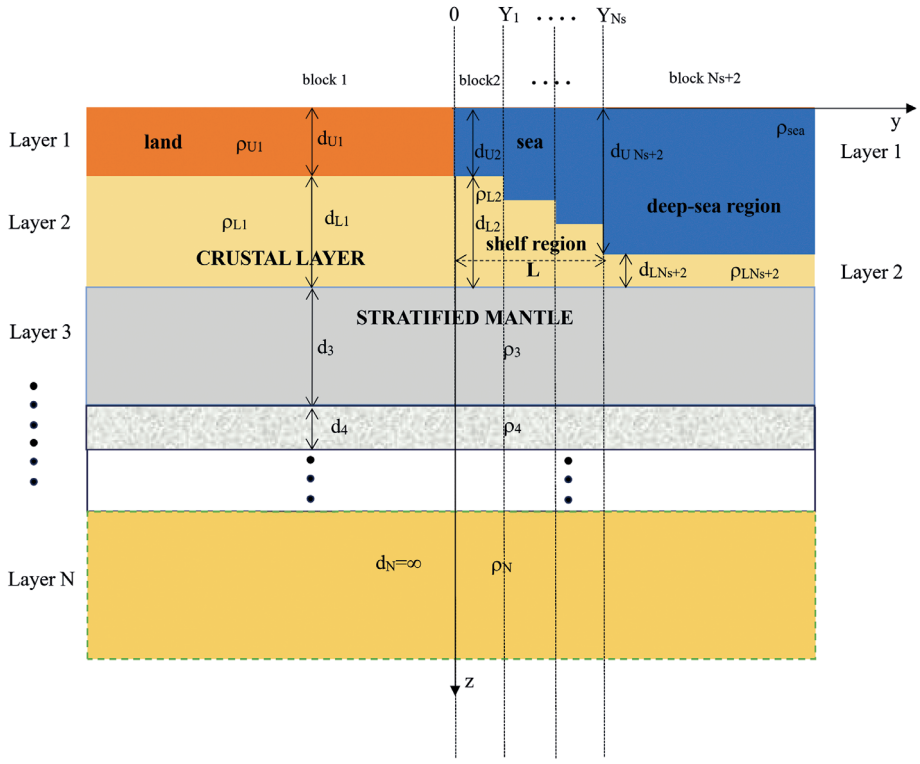

Fig. 1 - Earth stratification and stepped-depth sea models. The left side represents the land whose first conductive layer is generally composed of sediments, while, the right side represents the space occupied by the sea whose first layer is the seawater. In turn, the seawater region is subdivided into two parts: in the first, the depth is not constant and represents the shelf region, whereas in the second, the depth is constant and maximum and represents the deep-sea region. On both left and right sides, below the first layer, lies the second resistive layer given by the crust, under which there is a stratified mantle composed of *N*-2 layers, with the last one having an infinite depth.

crustal layer (layer 2) to have the same resistivity on the left and on the right side with respect to the coast and the same holds for the resistivities and thicknesses of the layers forming the mantle (layers from 3 to *N*).

Along the horizontal *y*-axis from left to right, we may subdivide the *N* vertical layers composing the Earth's structure into *Ns*+2 blocks where *Ns* is the number of steps (or equivalent layers with different depths) characterising the sea model in the shelf region. The transition between two consecutive blocks is obtained at coordinates 0, Y_1, …Y_{Ns}, therefore, they represent *Ns*+1 points of discontinuity for the model. Moreover, each block is characterised by *N* vertical layers each characterised, in turn, by resistivity and thickness. The first block on the land side (block 1 in Fig. 1) and the last one on the sea side, i.e. the deep-sea region (block *Ns*+2 in Fig. 1), have infinite extension also in the horizontal direction (i.e. along the *y* axis).

For the generalised thin sheet model to be applied, the thickness of the first and second layers of each block must be smaller than the skin depth in those layers (Wang *et al*., 2023) so that the electromagnetic fields penetrate through both of the first two layers. In practice, it is assumed that electric field *E* does not vary substantially with depth across the first layer, while magnetic field *H* does not vary substantially with depth across the second layer. This results in a limitation in frequencies and layer thicknesses when using the generalised thin sheet model. Nevertheless, the range of frequencies typically involved in the geoelectric induction phenomenon (0.1-100 mHz) enables us to use it, exception made for the case of very deep seas.

The last hypothesis, adopted in the present paper, concerns the polarisation of the electromagnetic field which is assumed as modelled by a uniform plane wave, which is vertically incident on the Earth's surface, represented by the H-polarised *xy* plane, as shown in Fig. 2 (top right).

The choice of considering this specific polarisation is motivated by the fact that, as largely mentioned in literature, it results in the maximum geoelectric coast effect. Therefore, producing the maxima GICs on the infrastructures which are located not far from the coast (see Appendix A for more details).

3. Time-domain analytical expression of the incident geomagnetic field

Since the main goal of this study is to make a prediction of the geoelectric field, it is worthwhile to start by adopting a convenient expression that represents the incident magnetic field in the time domain.

Pirjola and Boteler (2017), Boteler and Pirjola (2019), and Boteler *et al*. (2019) proposed a synthetic magnetic field expression in the time domain that can be used as a credible proxy for a real geomagnetic disturbance. The same expression has also been used by Wang *et al*. (2021) in a more recent work.

The formula proposed is:

$$H(t) = \frac{1}{\mu_0} \sum_{m=1}^{7} A_m \sin(2\pi f_m t + \Phi_m) \tag{1}$$

where μ_0 is the vacuum absolute magnetic permeability and the quantities A_m, f_m, and Φ_m are defined in Table 1.

According to the hypothesis of H polarisation, introduced in the previous section, we assume

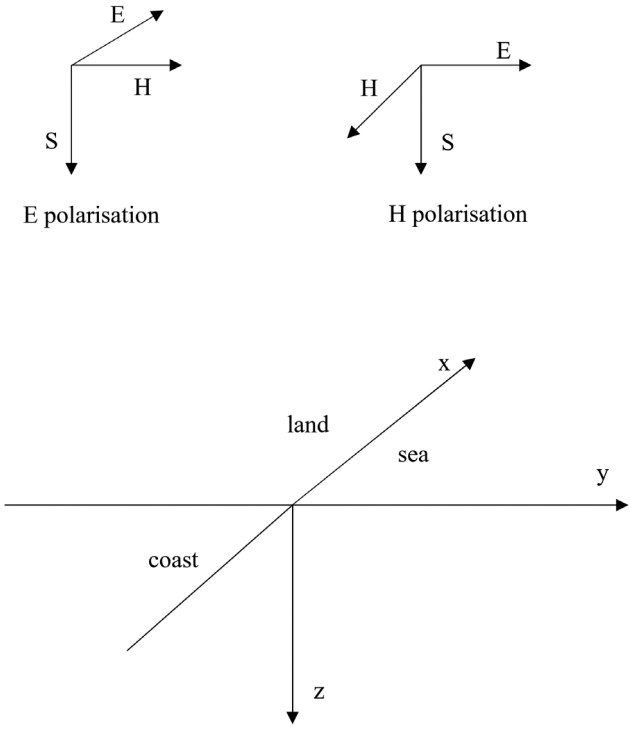

Fig. 2 - Scheme of E polarisation (top left) and H polarisation (top right) of a plane wave normally incident on the Earth's surface represented by the *xy* plane; S is the Poynting vector and the *xz* plane represents the land/sea discontinuity.

Table 1 - Parameters used for the synthetic geomagnetic field expression.

m	A_m (nT)	Φ_m (deg)	f_m (Hz)
1	200	10	0.00009259
2	90	20	0.000208333
3	30	30	0.00047619
4	17	40	0.00111111
5	8	50	0.00238095
6	3.5	60	0.00555555
7	1	70	0.0025

that the incident magnetic field only has the *x* component described by Eq. (1).

Boteler *et al*. (2019) observed that the waveshape described by Eq. (1), if amplified by a factor of 30, enables to reproduce the calculated geoelectric field, using the Quebec Earth model that has been generated during the, often mentioned in literature, geomagnetic storm of 13 March 1989.

In principle, the proposed method, described in the next section, can be applied to any time series registration of geomagnetic field whose time histories are available at http://www.intermagnet.org and http://supermag.jhuapl.edu. The results discussed in Section 5 have been obtained by applying Eq. (1).

4. Calculation of the geoelectric field

This section is devoted to the outlining of the calculation method of the geoelectric field, $E(y,f) = E_y(y,f)$, first in the frequency domain and, then, in the time domain by means of the Inverse Fourier Transform.

By extending the results of Ranganayaki and Madden (1980) (also see Gummow *et al*., 2002), the differential equation that describes the electric field at the ground surface in each of the blocks as represented in Fig. 1 is:

$$\frac{d^2E_i(y,f)}{dy^2} - \frac{1}{\tau_i\lambda_i}E_i(y,f) = -\frac{E_i^0(f)}{\tau_i\lambda_i} \qquad i = 1, 2, \ldots Ns+2 \qquad (2)$$

where $\tau_i = \sigma_{Ui}d_{Ui}$, $\lambda_i = \rho_{Li}d_{Li}$, and $E_i^0(f)$ (i = 1,2,…Ns+2) represent the incident electric field at large distance from the discontinuities so that their effect can be considered negligible. According to Fig. 1, the symbols σ_{Ui} (with $\sigma_{Ui} = 1/\rho_{Ui}$) and d_{Ui} represent the conductivity and thickness of the upper layer belonging to the i-th block while ρ_{Li} and d_{Li} represent the resistivity and thickness of the lower layer belonging to the i-th block.

Let us define by $H^0(f)$ the incident magnetic field that we assume constant all over the area under study. The incident electric field, $E^0_i(f)$, is related to $H^0(f)$ by the following equation:

$$E_i^0(f) = -Z_{Ti}(f)H^0(f) \qquad i = 1, 2, \ldots Ns+2 \qquad (3)$$

where $Z_{Ti}(f)$ is the surface impedance relevant to the i-th block evaluated far from the discontinuities so that their effect can be neglected. The surface impedance, $Z_{Ti}(f)$, can be calculated by means of a recursive relation according to Trichtchenko and Boteler (2002).

The solution of Eq. (2) is found by considering that, for $y \to \pm\infty$, electric field $E(f)$ must vanish and by imposing the continuity conditions for quantities $\tau_i E_i$ and $\tau_i\lambda_i(\partial E/\partial y)$ (Ranganayaki and Madden, 1980) at the boundary between any two consecutive blocks, i.e. at the point of abscissa 0, $Y_1, \ldots, Y_{Ns}$.

Thus, if $Ns \geq 2$, we obtain:

$$E(y,f) = \begin{cases} C_1(f)e^{\frac{y}{\sqrt{\tau_1\lambda_1}}} + E_1^0(f) & y \leq 0 \\ C_2(f)e^{\frac{-y}{\sqrt{\tau_2\lambda_2}}} + C_3(f)e^{\frac{y}{\sqrt{\tau_2\lambda_2}}} + E_2^0(f) & 0 < y \leq Y_1 \\ C_{2i-2}(f)e^{\frac{-y}{\sqrt{\tau_1\lambda_1}}} + C_{2i-1}(f)e^{\frac{y}{\sqrt{\tau_1\lambda_1}}} + E_i^0(f) & Y_{i-2} < y \leq Y_{i-1} \quad i = 3,4 \ldots Ns \\ C_{2Ns+2}(f)e^{\frac{-y}{\sqrt{\tau_{Ns+2}\lambda_{Ns+2}}}} + E_{Ns+2}^0(f) & y > Y_{Ns} \end{cases} \qquad (4a)$$

While, if Ns = 1, we obtain:

$$E(y,f) = \begin{cases} C_1(f)e^{\frac{y}{\sqrt{\tau_1\lambda_1}}} + E_1^0(f) & y \leq 0 \\ C_2(f)e^{\frac{-y}{\sqrt{\tau_2\lambda_2}}} + C_3(f)e^{\frac{y}{\sqrt{\tau_2\lambda_2}}} + E_2^0(f) & 0 < y \leq Y_1 \\ C_4(f)e^{\frac{-y}{\sqrt{\tau_3\lambda_3}}} + E_3^0(f) & y > Y_1 \end{cases} \qquad (4b)$$

Coefficients $C_i(f)$ are the solution of the following linear system:

$$[M][C(f)] = [T(f)] \tag{5}$$

where [*M*] is a constant square matrix of order 2*Ns* + 2 defined in Appendix B while [*C(f)*] is the unknown vector of order 2*Ns*+2 and [*T(f)*] is the driving terms vector of order 2*Ns*+2 given by:

$$[T(f)] = \begin{bmatrix} -\tau_1 E_1^0(f) + \tau_2 E_2^0(f) \\ 0 \\ -\tau_2 E_2^0(f) + \tau_3 E_3^0(f) \\ 0 \\ \vdots \\ -\tau_{Ns+1} E_{Ns+1}^0(f) + \tau_{Ns+2} E_{Ns+2}^0(f) \\ 0 \end{bmatrix}. \tag{6}$$

Once vector [*C(f)*] has been determined, we are particularly interested in the geoelectric field on the land side that is given by the top expression in Eqs. (4); we can notice that the electric field attenuates exponentially as one moves away from the coast and the frequency is involved only in coefficient $C_1(f)$ and in driving term $E^0{}_1(f)$ but not in the exponential term that only depends on the characteristics of the upper and lower layers (conductivity and thickness) on the land side.

It is also useful to note that this exponential term is identical to the one which can be found in the analogous expression for the simpler constant-depth sea case (see Ranganayaki and Madden, 1980; Gummow *et al*., 2002; Lucca, 2024). From this, we can deduce that the presence of the shelf region only influences the magnitude of the electric field on the land side but not on its attenuation rate.

We can also define the Earth's transfer function (on the land side), $K(y, f)$, with the following equation:

$$K(y,f) = \frac{C_1(f) e^{\frac{y}{\sqrt{\tau_1 \lambda_1}}} + E_1^0(f)}{\mu_0 H^0(f)} \qquad y \leq 0. \tag{7}$$

Therefore, thanks to knowledge of the magnetic field $H(t)$ in the time domain and of the Earth's transfer function $K(y, f)$ in the frequency domain, the electric field $E(t)$ in the time domain can be obtained through the following three steps:

1) calculation of magnetic field $H(f)$ in the frequency domain by means of the Fourier Transform of $H(t)$;
2) calculation of the electric field in frequency domain $E(y, f)$ by multiplying each frequency component of $H(f)$ by the Earth's transfer function, $K(y, f)$, evaluated at the same frequency;
3) calculation of the electric field in time domain $E(y, t)$ by means of the Inverse Fourier Transform of $E(y, f)$.

5. Results

In this section, the results obtained by applying the previously outlined calculation method are presented. This method consists in varying some of the influencing parameters of the model,

such as shelf length *L*, deep-sea region depth, shelf slope, and distance from the coastline while the other data regarding the Earth stratification model are kept constant.

Table 2 shows the values of the resistivities and thicknesses used in the present work; by choosing these values, we adopted an Earth stratification model that is mostly based on the one presented by Chakraborty *et al*. (2022) and Boteler *et al*. (2023), who, in turn, grounded their work on the LITHO1.0 model (Pasyanos *et al*., 2014) which gives an updated crust and lithospheric representation of the Earth.

Table 2 - The Earth resistivity model used in this work.

Land side			**Sea side**		
Description	***d* (km)**	**ρ (Ωm)**	**Description**	***d* (km)**	**ρ (Ωm)**
Sediments	0.05	50	Seawater	More than one value	0.3
Crust	10	3000	Crust	10	3000
Mantle lithosphere	140	1000	Mantle lithosphere	140	1000
Upper mantle	247	100	Upper mantle	247	100
Transition zone	250	10	Transition zone	250	10
Lower mantle	∞	1	Lower mantle	∞	1

Considering other parameters characterising the model, according to Mosetti (1979), in many cases shelf extension *L* can be of some tens of kilometres, but it may also reach some hundreds of kilometres.

As far as the slope of the coast is concerned, we considered values reported in the EPRI (2020) relevant to U.S. coasts where most of them lie within the range of [0.01°, 0.5°]. In addition, in the context of our paper, the coast slope angle, θ, is defined by $\theta=atan(L/D_{ds})$ where D_{ds} is the depth in the deep-sea region.

Regarding the depth of the deep-sea region, we considered a maximum value for D_{ds} of 600 m to satisfy the constraint related to the generalised thin sheet model explained in Section 2. This because, in the range of frequencies involved in the phenomenon, the thickness of the first and second layers of each block must be smaller than the skin depth in those same layers (Wang *et al*., 2023).

We assumed an incident magnetic field, *H(t),* defined according to Eq. (1) having a duration of three days and sampling interval of one minute. According to Boteler and Pirjola (2019), before taking the Fast Fourier Transform (FFT) of the signal, the time series was tapered at its ends by means of a split cosine bell window to prevent spurious frequencies from being introduced by the discontinuities represented given by the ends of the time series itself. Finally, to minimise the influence of the tapering on the results of the geoelectric field obtained by the inverse FFT, they are presented only for the central day (i.e. the second one), thus disregarding the first and third days.

In Fig. 3, the geoelectric field evaluated by means of the stepped-depth sea model for different *L* values is compared with the corresponding field obtained by means of a constant-depth sea model. The shelf has been divided into three steps of equal length having depths of 30 m, 60 m, and 90 m, respectively, and the field has been evaluated at 100 m from the coast. Overall, depending on the value of *L*, the stepped-depth sea model gives results in amplitude that may be greater or smaller than the ones obtained by the constant-depth sea model. In Fig. 3, it is also

drawn the geoelectric field evaluated very far from the coastline so that the geoelectric coast effect is completely attenuated, thus, we may observe the large difference between the fields when considering or not the geoelectric coast effect. In fact, by looking at the plot (in green), evaluated very far from the coast, we can see that its fluctuations are in a range of magnitude much smaller than the other plots (blue, red, and black) obtained, instead, by considering the coast effect. To better highlight, in a quantitative way, the differences between the geoelectric field evaluated in the four different cases of Fig. 3, in Table 3 the maximum and minimum values of the field itself are shown.

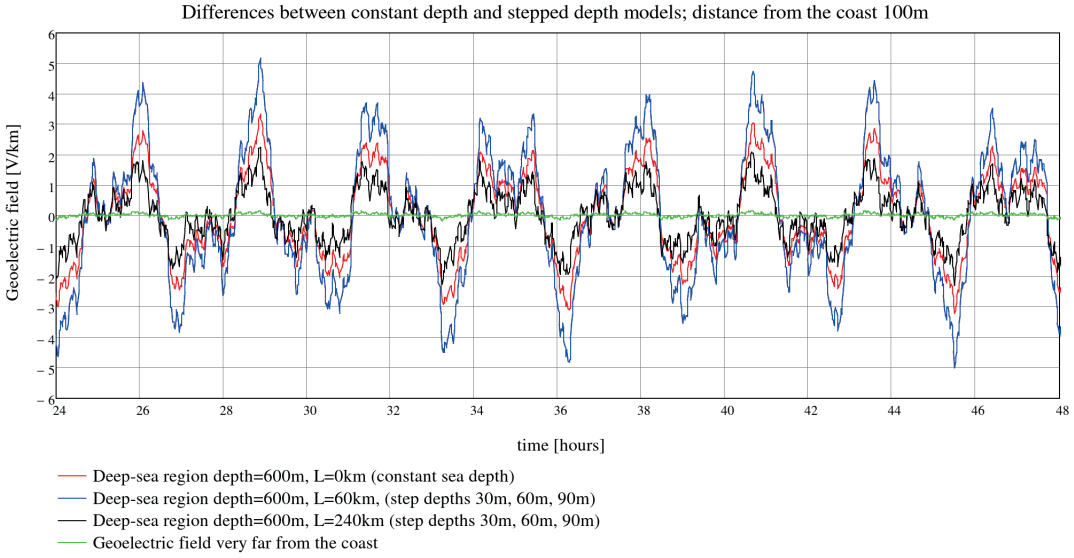

Fig. 3 - Comparison between the geoelectric field evaluated by means of the stepped-depth sea model and the constant-depth sea model. In order to appreciate the importance of the geoelectric coast effect, the geoelectric field very far from the coast, where this effect has vanished, is also included.

Table 3 - Maximum and minimum values of the geoelectric field shown in Fig. 3.

	E **[V/km]** ***L*** **= 60 km**	***E*** **[V/km]** ***L*** **= 0 km (constant sea depth)**	***E*** **[V/km]** ***L*** **= 240 km**	***E*** **[V/km] no coast effect**
Maximum	5.152	3.318	2.304	0.181
Minimum	-5.019	-3.217	-2.294	-0.17

In Fig. 4, the different plots of the geoelectric field, for different values of shelf length *L* and at a distance from the coast of 100 m, are shown; the shelf has been divided into three steps of equal length, with depths of 30 m, 60 m, and 90 m, respectively, while the deep-sea region depth is 600 m. We can notice that the geoelectric field increases in amplitude when shelf length *L* decreases; this can be explained by observing that the larger the shelf width length, the higher the leakage current to the mantle, thus resulting in lower levels of magneto-telluric current migrating from sea to land and, consequently, also in lower geoelectric field levels. To better highlight, in a quantitative way, the differences between the geoelectric field evaluated in the four different cases of Fig. 4, in Table 4 the maximum and minimum values of the field itself are shown.

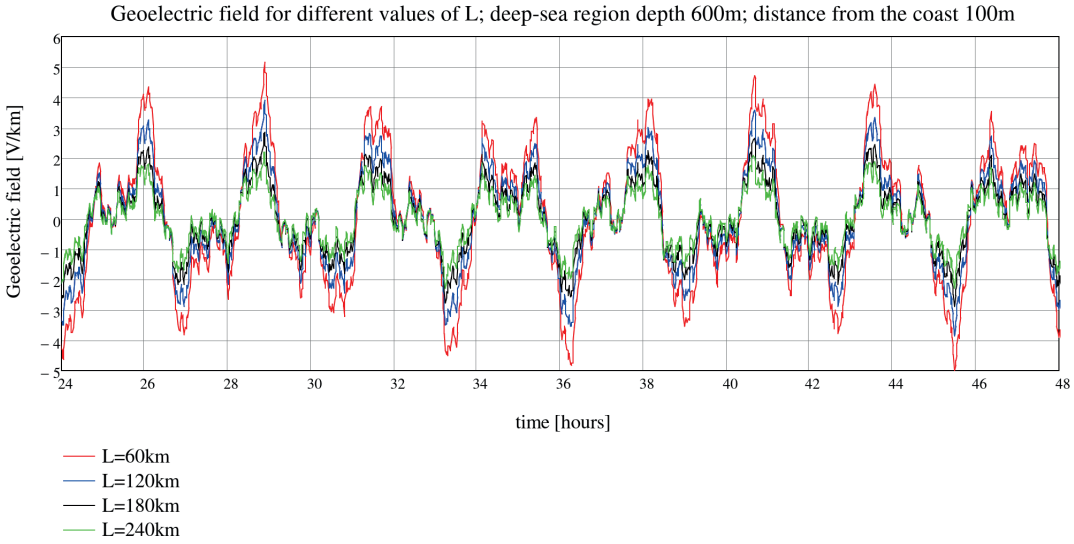

Fig. 4 - The geoelectric field obtained for different *L* values at a distance from the coast of 100 m and for a deep-sea region depth of 600 m.

Table 4 - Maximum and minimum values of the geoelectric field shown in Fig. 4.

	***E* [V/km] *L* = 60 km**	***E* [V/km] *L* = 120 km**	***E* [V/km] *L* = 180 km**	***E* [V/km] 240 km**
Maximum	5.152	3.887	2.86	2.304
Minimum	-5.019	-3.857	-2.899	-2.294

In Fig. 5, different plots of the geoelectric field, for different values of the deep-sea region depth and at distance of 100 m from the coast, are shown; the shelf has been divided into three

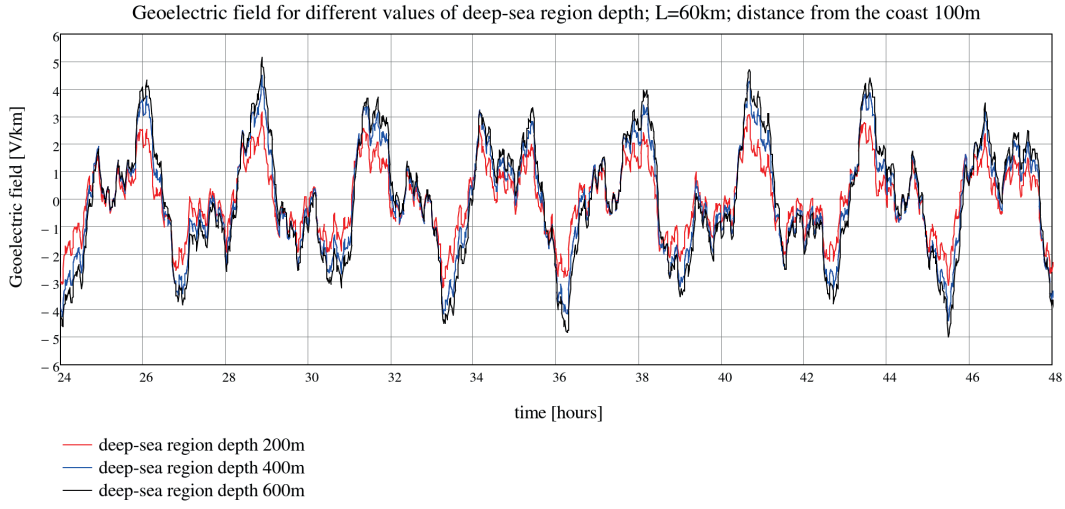

Fig. 5 - The geoelectric field obtained for different values of deep-sea depth at a distance from the coast of 100 m and for *L* = 60 km.

steps of equal length, with depths of 30 m, 60 m, and 90 m, respectively, while the shelf has a length L = 60 km. In this case, the higher the deep-sea region depth, the higher the geoelectric field amplitude. To better put in evidence, in a quantitative way, the differences between the geoelectric field evaluated in the three different cases of Fig. 5, in Table 5 the maximum and minimum values of the field itself are shown.

Table 5 - Maximum and minimum values of the geoelectric field shown in Fig. 5.

	E **[V/km] deep-sea region depth 200 m**	***E*** **[V/km] deep-sea region depth 400 m**	***E*** **[V/km] deep-sea region depth 600 m**
Maximum	3.338	4.511	5.152
Minimum	-3.193	-4.407	-5.019

Additionally, the influence of the shelf region slope on the geoelectric field is shown; by considering a shelf region with a length of L = 60 km subdivided into three steps of equal length and considering three different slopes:

1) slope 1 with depths 25, 50, and 75 m (i.e. 75 m/60 km);
2) slope 2 with depths 50, 100, and 150 m (i.e. 150 m/60 km);
3) slope 3 with depths 100, 200, and 300 m (i.e. 300 m/60 km).

The geoelectric field has been evaluated at 100 m from the coast and is shown in Fig. 6 for the three different cases. It is evident in Fig. 6 that the lower the shelf region slope, the higher the geoelectric field amplitude. To better highlight, in a quantitative way, the differences between the geoelectric field evaluated in the three different cases of Fig. 6, in Table 6 the maximum and minimum values of the field itself are shown.

Finally, to analyse field attenuation when moving away from the coast, in Fig. 7 the field is shown for distances of 100, 1000, and 10,000 m and, as a reference, the plot of the field very far from the coast is also added. Fig. 7 shows how the geoelectric coast effect manifests itself even at tens of kilometres from the coast line or even more; such a distance depends on the known as the

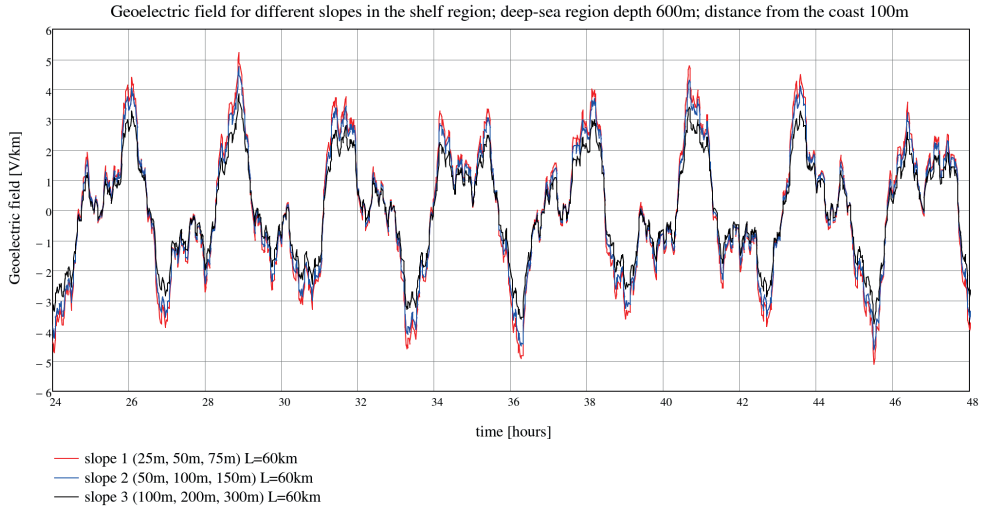

Fig. 6 - The geoelectric field obtained for different values of the shelf region slope at a distance from the coast of 100 m and for L = 60 km.

Table 6 - Maximum and minimum values of the geoelectric field shown in Fig. 6.

	***E* [V/km] slope 75 m/60 km**	***E* [V/km] slope 150 m/60 km**	***E* [V/km] slope 300 m/60 km**
Maximum	5.232	4.763	3.853
Minimum	-5.1	-4.638	-3.763

'adjustment distance', $d_{adj}=(\sigma_{U1}d_{U1}\rho_{L1}d_{L1})^{1/2}$, [see the top equation in Eqs. (4a) and (4b)] which in turn depends on the conductivity and thickness values of the first two layers on the land side. To better put in evidence, in a quantitative way, the differences between the geoelectric field evaluated in the four different cases of Fig. 7, in Table 7 the maximum and minimum values of the field itself are shown. Looking at Table 7, it is remarkable to notice how even at a distance equal to 10 km from the coast, the maximum and minimum of the field are about five times higher than the corresponding values assumed by ignoring the geoelectric coast effect; more in general, from a practical point of view, the geoelectric coast effect vanishes at a distance from the coastline equal to $4d_{adj.}$

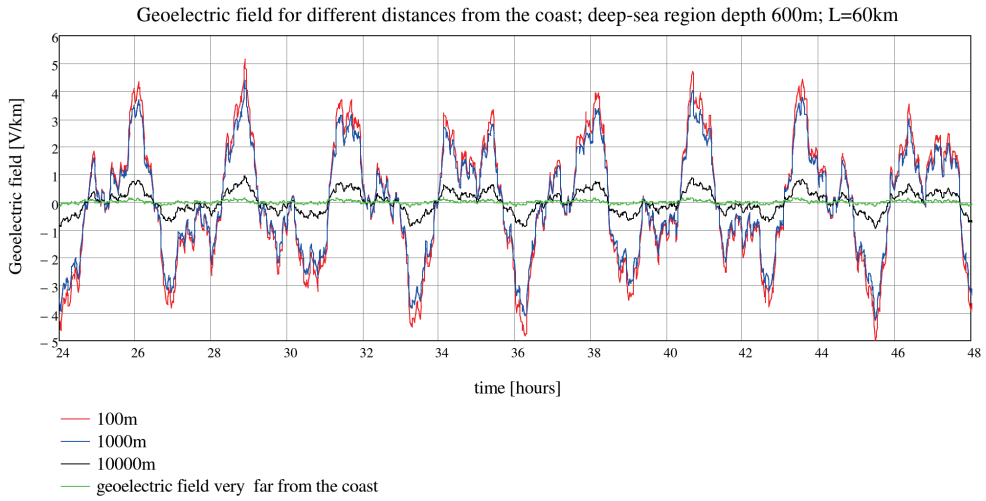

Fig. 7 - Comparison between the geoelectric field evaluated at different distances from the coast; the graph of the geoelectric field very far from the coast, where this effect has vanished, is also included as a reference.

Table 7 - Maximum and minimum values of the geoelectric field shown in Fig. 7.

	***E* [V/km] *y* = 100 m**	***E* [V/km] *y* = 1000 m**	***E* [V/km] *y* = 10000 m**	***E* [V/km] no coast effect**
Maximum	5.152	4.391	0.953	0.181
Minimum	-5.019	-4.282	-0.953	-0.17

6. Conclusions

In this paper, we have presented a 2D calculation method for the evaluation of the geoelectric coast effect and aimed to the assessment of a GIC on technological infrastructures located not far

from a coastline. The calculation method is based on the generalised thin sheet model and the main aspect of novelty is the stepped-depth sea representation instead of the classical constant-depth sea approach.

The results presented in this paper highlight that the presence of an intermediate region (shelf region), between a land region and a deep-sea region, significantly influence the amplitude of the geoelectric field. Particularly, such amplitude increases where shelf length *L* and shelf slope decrease and the deep-sea region depth increases.

Nevertheless, as highlighted in Section 4, it is necessary to remark that the presence of the shelf region, interposed between the land region and the deep-sea region, does not influence the electric field attenuation rate with distance from the coast with respect to the simpler constant-depth sea model. At the same time, we cannot conclude that taking into account the shelf region in the model always yields larger electric fields than the simpler constant-depth sea model.

The main drawback of this approach is represented by the applicability to not very deep seas, while the main advantage is its capability of modelling the sea structure in a quite simple and more realistic way. Therefore, some important and influencing factors, that are not present in the simpler constant-depth sea model, can hopefully be considered a beneficial improvement in the assessment of GICs in exposed infrastructures. Another advantage is represented by the reduced computational burden requested by the proposed method compared to other approaches (e.g. the FEM).

Possible future work will encompass the comparison of predicted electric fields with measured fields and/or results coming from other models, the extension of the present model to the more general case of mixed E and H polarisation and the modelling, and the assessment of GICs in technological structures located in coastal regions.

Acknowledgments. The author wishes to thank the anonymous reviewers and the editor for their helpful remarks and suggestions that enabled the paper to be improved.

REFERENCES

Blake J.R.; 1968: *The influence of coastal and see floor geometry on natural electromagnetic variations of 10^{-4} to 10^{3} Hz*. PH.D. Thesis in Physics, University of Alaska, Alaska, AK, USA, 188 pp.

Boteler D.H.; 2001a: *Assessment of geomagnetic hazard to power system in Canada*. Nat. Hazards, 23, 101-120, doi: 10.1023/A:1011194414259.

Boteler D.H.; 2001b: *Geomagnetic hazards*. In: Brooks G.R. (ed), A synthesis of geological hazards in Canada, Geological Survey of Canada, Bull. 548, pp. 183-206, doi: 10.4095/212210.

Boteler D.H.; 2003: *Geomagnetic hazards to conducting networks*. Nat. Hazards, 28, 537-561, doi: 10.1023/A:1022902713136.

Boteler D.H. and Pirjola R.J.; 2019: *Numerical calculation of geoelectric fields that affect critical infrastructure*. Int. J. Geosci., 10, 930-949, doi: 10.4236/ijg.2019.1010053.

Boteler D.H., Pirjola R.J. and Marti L.; 2019: *Analytic calculation of geoelectric fields due to geomagnetic disturbances: a test case*. IEEE Access, 7, 147029-147037, doi: 10.1109/ACCESS.2019.2945530.

Boteler D.H., Chakraborty S., Shi X., Hartinger M.D. and Wang X.; 2023: *Transmission line modelling of geomagnetic induction in the ocean/Earth conductivity structure*. Int. J. Geosci., 14, 767-791, doi: 10.4236/ijg.2023.148041.

Chakraborty S., Boteler D.H., Shi X., Murphy B.S., Murphy B.S., Hartinger M.D., Wang X., Lucas G. and Baker J.B.H.; 2022: *Modeling geomagnetic induction in submarine cables*. Front. Phys., 10, doi: 103389/fphy.2022.1022475

d'Erceville I. and Kunetz G.; 1962: *The effect of a fault on the Earth's natural electromagnetic field*. Geophys., 27, 651-665, doi: 10.1190/1.1439075.

Dong B., Wang Z., Pirjola R., Liu C. and Liu L.; 2015a: *An approach to model Earth conductivity structures with lateral changes for calculating induced currents and geoelectric fields during geomagnetic disturbances*. Math. Problems in Engineering, 2015, 761964, 1-10, doi: 10.1155/2015/761964.

Dong B., Wang Z., Liu L.G., Liu L.P. and Liu C.M; 2015b: *Proximity effect on the induced geoelectric field at the lateral interface of different conductivity structures during geomagnetic storms*. Chin. J. Geophys., 58, 32-40, doi: 10.1002/cjg2.20153.

EPRI (Electric Power Research Institute); 2020: *Nonuniform field modeling: coast effect assessment*. EPRI Report, 64 pp., <www.epri.com/research/products/000000003002017898>.
Fischer G.; 1979. *Electromagnetic induction effects at an ocean coast*. Proc. IEEE, 67, 1050-1060, doi: 10.1109/PROC.1979.11388.
Gilbert J.L.; 2005: *Modeling the effect of the ocean-land interface on induced electric fields during geomagnetic storms*. Space Weather, 3, S04A03, doi: 10.1029/2004SW000120.
Gummow R.A., Boteler D.H. and Trichtchenko L.D.; 2002: *Telluric and ocean current effects on buried pipelines and their cathodic protection systems*. Pipeline Research Council International, Inc., 148 pp., <ostrnrcan-dostrncan.canada.ca/handle/1845/160064>.
Liu C., Wang X., Wang H. and Zhao H.; 2018: *Quantitative influence of coast effect on geomagnetically induced currents in power grids: a case study*. J. Space Weather Space Clim., 8, A60, 1-9, doi: 10.1051/swsc/2018046.
Lucca G.; 2024: *Induced geoelectric field: influence of polarization in coast effect and proximity effect*. Ann. Geophys., 67, SA549, doi: 10.4401/ag-9107.
Mosetti F.; 1979: *Fondamenti di oceanologia e idrologia*. UTET, Torino, Italy, 603 pp.
Pasyanos M.E., Masters T.G., Laske G. and Ma Z.; 2014: *Litho1.0: an updated crust and lithospheric model of the Earth*. J. Geophys. Res.: Solid Earth, 119, 2153-2173, doi: 10.1002/2013JB010626.
Pilipenko V.A.; 2021: *Space weather impact on ground-based technological systems*. Sol. Terr. Phys., 7, 68-104, doi: 10.12737/stp-73202106.
Pirjola R.J. and Boteler D.H.; 2017: *Truncation of the Earth impulse responses relating geoelectric fields and geomagnetic field variations*. Geosci. Res., 2, 72-92, doi: 10.22606/gr.2017.22002.
Pokhrel S., Nguyen B., Rodriguez M., Bernabeu E. and Simpson J.J.; 2018: *A finite difference time domain investigation of electric field enhancements along ocean-continent boundaries during space weather events*. J. Geophys. Res. Space Phys., 123, 5033-5046, doi: 10.1029/2017JA024648.
Ranganayaki R.P. and Madden T.R.; 1980: *Generalized thin sheet analysis in magnetotellurics: an extension of Price's analysis*. Geophys. J. Int., 60, 445-457, doi: 10.1111/j.1365-246X.1980.tb04820.x.
Rankin D.; 1962: *The magneto telluric effect on a dike*. Geophys., 27, 666-676, doi: 10.1190/1.1439077.
Trichtchenko L. and Boteler D.H.; 2002: *Modelling of geomagnetic induction in pipelines*. Ann. Geophys., 20, 1063-1072, doi: 10.5194/angeo-20-1063-2002.
Wang X., Liu C. and Kang Z.; 2021: *Effect of the Earth's lateral conductivity variations on geomagnetically induced currents in power grids*. Int. J. Electr. Power Energy Syst., 132, 107-148, doi: 10.1016/j.ijepes.2021.107148.
Wang X., Boteler D.H. and Pirjola R.J.; 2023: *Distributed-source transmission line theory for modeling the coast effect on geoelectric fields*. IEEE Trans. Power Delivery, 38, 3541-3550, doi: 10.1109/TPWRD.2023.3279462.
Weaver J.T.; 1963: *The electromagnetic field within a discontinuous conductor with reference to geomagnetic micropulsations near a coastline*. Can. J. Phys., 41, 484-495, doi: 10.1139/p63-051.
Weaver J.T.; 1994: *Mathematical methods for geo-electromagnetic induction*. Research Studies Press Ltd, Taunton, UK, 316 pp.

Corresponding author: Giovanni Lucca
Independent Researcher
29122 Piacenza, Italy
E-mail: vanni.luccapc@gmail.com

Appendix A

To start, E and H polarisation should be defined. To this purpose, the source geomagnetic field, represented by a plane wave normally incident to the *xy* plane representing the air-land/sea interface, should be considered. E or H polarisation occurs when the incident magnetic field is perpendicular or parallel to the coastline (see Fig. 2).

In general, the incident geomagnetic field is characterised by mixed polarisation i.e. it has both E and H polarised components that depend on polarisation angle Ψ which is defined with the help of Fig. A1.

We can notice that when:

- $\Psi = 0^0$ or $\Psi = 180^0$, E polarisation is obtained;
- $\Psi = 90^0$ or $\Psi = 270^0$, pure H polarisation is obtained.

From the GIC calculation point of view, the worst case occurs when the incident geomagnetic field is H polarised (Lucca, 2024). On the ground of Lucca (2024), we present in Fig. A2 some plots of the induced geoelectric field versus the distance from the coastline evaluated for different values of polarisation angle Ψ and for the typical frequency of f = 1 mHz that lies inside the spectrum characterising the phenomenon of the geoelectric induction; for other values of frequency, the qualitative trend of the curves, shown in Fig. A2, is also the same but for brevity reasons they have not been shown.

We can notice that, on the land side, the highest values of the field are in correspondence of $\Psi = 90^0$, i.e. the case of pure H polarisation. This justifies the choice of considering the specific case of H polarisation in the present work as worst-case scenario.

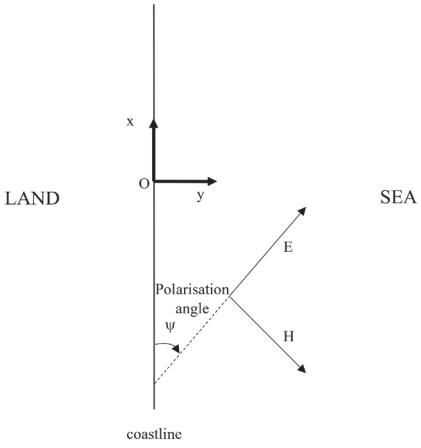

Fig. A1 - Definition of polarisation angle Ψ; when $\Psi = 0^0$ or $\Psi = 180^0$, pure E polarisation occurs, while, when $\Psi = 90^0$ or $\Psi = 270^0$, pure H polarisation occurs.

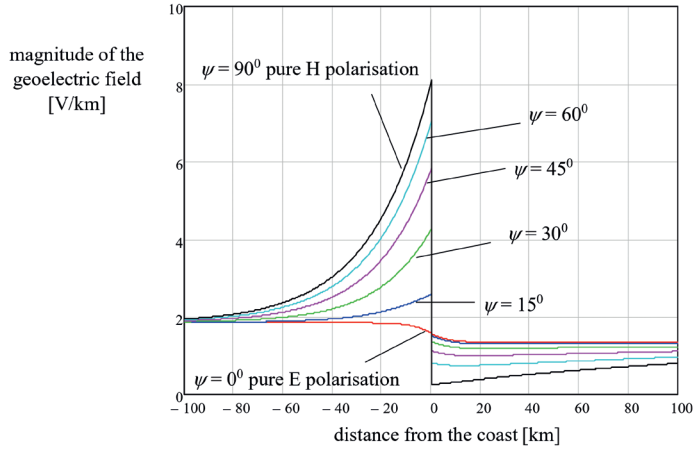

Fig. A2 - Magnitude of the induced geoelectric field, evaluated at the frequency of f = 1 mHz, versus the distance from the coast for different values of polarisation angle Ψ.

Appendix B

The full formulation for matrix [M], introduced in Section 4, is given as follows. If $Ns \geq 2$, it is convenient to consider [M] as a block matrix composed of Ns+1 different submatrices, [Mt], [M^1], [M^2],…[M^{Ns-1}] and [Mb], each of order 2 × (2Ns+2), that is:

$$[M] = \begin{bmatrix} [Mt] \\ [M^1] \\ [M^2] \\ \vdots \\ [M^{Ns-1}] \\ [Mb] \end{bmatrix}. \tag{B1}$$

The generic element of each of the above-mentioned submatrices are separately defined. Top submatrix [*Mt*] has order 2 × (2*Ns*+2) and the generic element is given by:

$$Mt_{i,j} = \begin{cases} \tau_1 & if \quad i=1 \quad j=1 \\ -\tau_2 & if \quad i=1 \quad j=2,3 \\ \sqrt{\tau_1\lambda_1} & if \quad i=2 \quad j=1 \\ \sqrt{\tau_2\lambda_2} & if \quad i=2 \quad j=2 \\ -\sqrt{\tau_2\lambda_2} & if \quad i=2 \quad j=3 \\ 0 & otherwise \end{cases} . \tag{B2}$$

The *k*-th submatrix, (*k* = 1, 2…*Ns*-1) [M^k], has order 2 × (2*Ns*+2) and the generic element is given by:

$$M_{i,j}^k = \begin{cases} \tau_{k+1}e^{\frac{-Y_k}{\sqrt{\tau_{k+1}\lambda_{k+1}}}} & if \quad j=2k \quad i=1 \\ \tau_{k+1}e^{\frac{Y_k}{\sqrt{\tau_{k+1}\lambda_{k+1}}}} & if \quad j=2k+1 \quad i=1 \\ -\tau_{k+1}e^{\frac{-Y_k}{\sqrt{\tau_{k+2}\lambda_{k+2}}}} & if \quad j=2k+2 \quad i=1 \\ -\tau_{k+1}e^{\frac{Y_k}{\sqrt{\tau_{k+2}\lambda_{k+2}}}} & if \quad j=2k+3 \quad i=1 \\ -\sqrt{\tau_{k+1}\lambda_{k+1}}e^{\frac{-Y_k}{\sqrt{\tau_{k+1}\lambda_{k+1}}}} & if \quad j=2k \quad i=2 \\ \sqrt{\tau_{k+1}\lambda_{k+1}}e^{\frac{Y_k}{\sqrt{\tau_{k+1}\lambda_{k+1}}}} & if \quad j=2k+1 \quad i=2 \\ \sqrt{\tau_{k+2}\lambda_{k+2}}e^{\frac{-Y_k}{\sqrt{\tau_{k+2}\lambda_{k+2}}}} & if \quad j=2k+2 \quad i=2 \\ -\sqrt{\tau_{k+2}\lambda_{k+2}}e^{\frac{Y_k}{\sqrt{\tau_{k+2}\lambda_{k+2}}}} & if \quad j=2k+3 \quad i=2 \\ 0 & otherwise \end{cases} . \tag{B3}$$

Bottom submatrix [*Mb*] has order 2 × (2*Ns*+2) and the generic element is given by:

$$Mb_{i,j} = \begin{cases} \tau_{Ns+1}e^{\frac{-Y_{Ns}}{\sqrt{\tau_{Ns+1}\lambda_{Ns+1}}}} & if \quad i=1 \quad j=2Ns \\ \tau_{Ns+1}e^{\frac{Y_{Ns}}{\sqrt{\tau_{Ns+1}\lambda_{Ns+1}}}} & if \quad i=1 \quad j=2Ns+1 \\ -\tau_{Ns+2}e^{\frac{-Y_{Ns}}{\sqrt{\tau_{Ns+2}\lambda_{Ns+2}}}} & if \quad i=1 \quad j=2Ns+2 \\ -\sqrt{\tau_{Ns+1}\lambda_{Ns+1}}e^{\frac{-Y_{Ns}}{\sqrt{\tau_{Ns+1}\lambda_{Ns+1}}}} & if \quad i=2 \quad j=2Ns \\ \sqrt{\tau_{Ns+1}\lambda_{Ns+1}}e^{\frac{Y_{Ns}}{\sqrt{\tau_{Ns+1}\lambda_{Ns+1}}}} & if \quad i=2 \quad j=2Ns+1 \\ \sqrt{\tau_{Ns+2}\lambda_{Ns+2}}e^{\frac{-Y_{Ns}}{\sqrt{\tau_{Ns+2}\lambda_{Ns+2}}}} & if \quad i=2 \quad j=2Ns+2 \\ 0 & otherwise \end{cases} . \tag{B4}$$

Finally, we add that, in the simpler case for *Ns* = 1, matrix [*M*] assumes the following form:

$$[M] = \begin{bmatrix} [Mt] \\ [Mb] \end{bmatrix}. \tag{B5}$$